AIAA 2000-1991

EVOLUTION OF ROTOR WAKE IN SWIRLING FLOW

Basman El-Hadidi[1] and Hafiz Atassi[2]
University of Notre Dame, Notre Dame, IN 46556
and
Edmane Envia[3] and Gary Podboy[4]
NASA Glenn Research Center, Cleveland, OH 44135

Abstract

A theory is presented for modeling the evolution of rotor wakes as a function of axial distance in swirling mean flows. The theory, which extends an earlier work to include arbitrary radial distributions of mean swirl, indicates that swirl can significantly alter the wake structure of the rotor especially at large downstream distances (i.e., for moderate to large rotor-stator spacings). Using measured wakes of a representative scale model fan stage to define the mean swirl and initial wake perturbations, the theory is used to predict the subsequent evolution of the wakes. The results indicate the sensitivity of the wake evolution to the intial profile and the need to have complete and consistent initial definition of both velocity and pressure perturbations.

Introduction

The advent of high bypass ratio turbofans has made rotor-stator interaction noise one of the major sources of aircraft engine noise. This is true whether one is concerned with the tone component or the broadband component of noise spectrum. Reduction of the rotor-stator interaction noise, therefore, has become an integral part of many engine noise reduction strategies. Naturally, the success of a reduction technique depends critically on how well the underlying mechanism of the noise generation is understood. It is generally agreed that the principal mechanism of rotor-stator interaction is the impingement of rotor flow unsteady perturbations on the downstream stator vanes. In the case of tone noise, the perturbations are the coherent (periodic) wakes of the rotor, and, in the case of broadband noise, they include flow turbulence ingested and/or produced by the fan.

Over the past few decades a number of analytical and numerical methods have been developed to predict the rotor-stator interaction noise by modeling the rotor wakes as specified upstream vortical perturbations and the stator as a 2D rectilinear, or a 3D annular, cascade of airfoils. For unloaded cascades, the common approach is to use linear unsteady aerodynamic theory wherein flow nonuniformities are treated as imposed upstream disturbances purely convected by a uniform mean flow but otherwise not affected by it (i.e., the frozen gust assumption). The noise field is then calculated as the farfield potential response of the cascade to the impinging vortical disturbances. For loaded cascades, methods based on the rapid distortion theory are used to account for the effect of mean flow distortion of the upstream disturbances. Both the wake evolution and radiated sound are then determined as part of the solution [1]. However, to date, only 2D versions of the theory have been implemented in practical noise computation schemes.

In both types of approaches the upstream and downstream mean flows are taken to be uniform. In this case, the modal composition of the duct acoustics, which depends only on the mean flow and duct geometry, can be readily determined. The magnitude of the acoustic modes, then, depends on the unsteady aerodynamic response of the cascade. For annular geometries, strip theory is often used to compute the cascade unsteady aerodynamics by treating the 3D response as an aggregate of 2D reponses at each radius strip (see, for example, [2]).

However, despite the obvious simplicity of the mathematical development when the mean

[1]Research Assistant, Member AIAA
[2]Viola D. Hank Professor, Fellow AIAA
[3]Research Engineer, Senior Member AIAA
[4]Research Engineer, Member AIAA

flow is assumed uniform, there are definite shortcomings in these types of approaches. This is mainly because the flow downstream of moderate to highly loaded fans show significant swirling motion. In fact, the swirl component of velocity, which depends on the radial distribution of the blade loading, tip speed and rotor cascade stagger, may be comparable to the axial component of velocity in these flows. Wakes and secondary flow nonuniformities, therefore, evolve in a swirling flowfield. The mean swirl produces centrifugal and Coriolis forces which affect the motion and structure of the perturbations present in the flow and couple the vortical, entropic and acoustic modes [3]. The magnitude and phase of the unsteady perturbations evolving in swirling flow are, therefore, constantly changing.

Essentially, mean swirl has three principal effects on the rotor-stator interaction noise. First, it affects the evolution of the rotor wakes downstream of the fan and, thus, changes the upwash velocity induced on the outlet guide vanes (OGV) [4]. Second, it modifies the aerodynamic and aeroacoustic response of the OGV [5]. Third, it changes the structure of the acoustic duct modes and their cut-off criterion [6, 7, 8].

In trying to address the first issue, Golubev and Atassi [4] considered a mean swirl consisting of free-vortex and rigid body rotation components. Their results indicate that the influence of swirl on the wake evolution depends on the particular radial distribution of swirl considered. For example, a free-vortex swirl distribution leads to algebraic growth of the wake perturbations. On the other hand, a general swirl distribution *may* lead to axial modulation, exponential growth or decay of the wake perturbations. There is some experimental evidence for growth of wake perturbation under certain conditions as shown by the data of Lakshminarayana [9] who measured an increase in the radial component of wake perturbation as a function of downstream distance. It should be emphasized that the growth or decay effect being discussed here is separate from the viscous decay effect which is always present in a real flow. The overall evolution of wake perturbations will depend on both these effects. However, in what follows we shall ignore the viscous decay effect with the understanding that one can account for it, at least approximately, using wake decay correlations that abound in the technical literature.

The objective of this paper is to examine the effects of mean flow swirl on the structure of the rotor wakes as they convect downstream. To this end, we first extend the analysis by Golubev and Atassi [4] to accommodate a general radial distribution of mean swirl present a model for the wake evolution. Second, flowfield measurements obtained at NASA Glenn Research Center for a typical fan stage scale model will be used to define the mean swirl and initial wake perturbations for use in the theory. Third, data-theory comparison of the wake evolution will be presented. Finally, the paper will conclude with a summary of important results.

Theoretical Model for the Wake Evolution

As stated earlier, the primary objective of the present paper is to account for the effect of mean flow swirl on the evolution of wake perturbations downstream of the fan. We are particularly interested in describing the modification of the structure of the perturbation flow as it evolves over a distance on the order of the mean duct radius r_m. It is therefore plausible to assume that the fluid is inviscid and non-heat conducting. In addition, we suppose that the flow velocity and pressure can be written as

$$\vec{V}(x,r,\theta,t) = \vec{U}(r) + \vec{u}(x,r,\theta,t), \quad (1)$$

$$p(x,r,\theta,t) = p_0(r) + p'(x,r,\theta,t), \quad (2)$$

where x and r are the axial and radial coordinates, respectively, θ is the circumferential angle, and t is the time. We further assume that $|\vec{u}(x,r,\theta,t)| \ll |\vec{U}(r)|$ and $|p'(x,r,\theta,t)| \ll |p_0(r)|$, and that the mean flow velocity has a zero radial component,

$$\vec{U}(r) = U_x(r)\vec{e}_x + U_s(r)\vec{e}_\theta, \quad (3)$$

where ($\vec{e}_x$, $\vec{e}_\theta$) are the unit vectors in the axial and tangential directions, respectively.

It is advantageous to represent the perturbation velocity as the sum of a vortical part, $\vec{u}^R$, and a potential part, $\nabla\phi$ [4],

$$\vec{u} = \nabla\phi + \vec{u}^R. \tag{4}$$

Substituting equations (1), (2) and (4) into the Euler equations we get

$$\frac{D_o\vec{u}^R}{Dt} + (\vec{u}^R \cdot \nabla)\vec{U} = -\left(\nabla \times \vec{U}\right) \times \nabla\phi, \tag{5}$$

$$\left(\frac{D_o}{Dt}\left(\frac{1}{c_o^2}\frac{D_o}{Dt}\right) - \frac{1}{\rho_o}\nabla\cdot(\rho_o\nabla)\right)\phi = \frac{1}{\rho_o}\nabla\cdot(\rho_o\vec{u}^R), \tag{6}$$

where the operator $\frac{D_o}{Dt}$ and the pressure are given by

$$\frac{D_o}{Dt} = \frac{\partial}{\partial t} + \vec{U}\cdot\nabla, \tag{7}$$

$$p' = -\rho_o\frac{D_o\phi}{Dt}. \tag{8}$$

Solution of equations (5) and (6) requires an appropriate set of initial and boundary conditions. The velocity components are specified at the inlet of the computational domain together with an impermeability condition on the walls of the duct. The pressure is specified at both the inlet and outlet of the domain.

Following [4], we write

$$\{\vec{u}^R, \phi\}(x,r,\theta,t) = \int_{-\infty}^{\infty}\sum_{m=-\infty}^{\infty}\{\vec{A}_m, \varphi_m\}(x,r) \times e^{i(-\omega t + m\theta + \alpha x)}d\omega, \tag{9}$$

where α is defined by

$$\frac{D_o}{Dt}(-\omega t + m\theta + \alpha x) = 0. \tag{10}$$

We begin by solving the homogeneous part of equation (5) which can be explicitly integrated using the initial data specified at $x = 0$. The solution, denoted as $\vec{u}_h^R$, is given by

$$\begin{aligned}
u_r^R &= \left[\begin{array}{c} A_{r_m}(0,r)\cos\left(\frac{\lambda x}{U_x}\right) + \\ \frac{\lambda}{\frac{d(rU_s)}{dr}}A_{\theta_m}(0,r)\sin\left(\frac{\lambda x}{U_x}\right)\end{array}\right]e^{i\sigma},\\
u_\theta^R &= \left[\begin{array}{c} A_{\theta_m}(0,r)\cos\left(\frac{\lambda x}{U_x}\right) - \\ A_{r_m}(0,r)\frac{\frac{d(rU_s)}{dr}}{\lambda}\sin\left(\frac{\lambda x}{U_x}\right)\end{array}\right]\frac{e^{i\sigma}}{r},\\
u_x^R &= \left[\begin{array}{c} A_{x_m}(0,r) + \\ r\frac{\frac{dU_x}{dr}}{\frac{d(rU_s)}{dr}}\left(u_{\theta_m}(x,r) - u_{\theta_m}(0,r)\right)\end{array}\right]e^{i\sigma},\\
\lambda &= \sqrt{\frac{1}{r^3}\frac{d}{dr}(rU_s)^2},
\end{aligned} \tag{11}$$

where $\sigma = \alpha x - \omega t + m\theta$. The parameter λ is significant, since it determines the flow stability. When λ is real, the flow is stable and, hence, wake perturbations remain bounded. However, when λ is imaginary, the flow can become unstable resulting in growing wake perturbations.

Next, equation (6) is discretized and solved numerically assuming $\vec{u}^R = \vec{u}_h^R$ on the right hand side. This provides the first iterative solution for ϕ.

A particular solution for the vortical velocity can then be calculated by solving,

$$\frac{D_o\vec{u}_p^R}{Dt} + (\vec{u}_p^R\cdot\nabla)\vec{U} = -\left(\nabla\times\vec{U}\right)\times\nabla\phi. \tag{12}$$

The vortical velocity is then given by $\vec{u}^R = \vec{u}_h^R + \vec{u}_p^R$.

Equations (5) and (6) are solved iteratively until appropriate convergence criteria are met for both $\nabla\phi$ and $\vec{u}^R$.

Boundary and Initial Conditions

The boundary and initial conditions necessary for carrying out the solution procedure are as follows:

- At the inlet, $x = 0$, we specify
  1. $\vec{u}_h^R = \vec{u}_{\text{initial}}$, i.e., the initial data given from the measurment.
  2. $\frac{\partial\psi}{\partial x} = \frac{-p'_{\text{initial}}}{\rho_o U_x}$.
  3. $\vec{u}_p^R = -\nabla\phi$.
- At the exit $x = L$, we take
  1. $\frac{\partial^2\psi}{\partial x^2} + \frac{\lambda^2}{U_x^2}\psi = 0$.
- On the tip and hub radii, we take
  1. $u_r^R + \frac{\partial\phi}{\partial r} = 0$,

where $\phi = \psi(x,r)e^{i\sigma}$. Often, the pressure is not measured at the inlet of the domain. As a result, the initial conditions for the pressure must be imposed artificially by assuming either $p = 0$ or $\frac{\partial p}{\partial x} = 0$.

Experimental Flowfield Measurement

The experimental wake data used in this paper were obtained at the NASA Glenn 9-foot x 15-foot Low Speed Wind Tunnel during testing of a high bypass ratio subsonic fan stage model which was designed and built by the Allison Engine Company. Figure (1) shows a photograph of this model installed in the tunnel. The fan has a diameter of 22 inches with 18 blades, a hub-to-tip radius ratio of $\sigma = 0.5$ and a design rotational speed of 10,400 RPM. A Laser Doppler Velocimeter (LDV) was used to map the velocity field downstream of the fan at three axial positions (locations 1, 2 and 3 shown in figure (2) corresponding to 1.2, 2.4, 3.4 inches downstream of the fan trailing edge, each at three different corrected fan speeds corresponding to the approach (5,200 RPM), cutback (8,900 RPM) and sideline (10,400 RPM) conditions. The LDV data was acquired with the stators mounted in the aft position as shown in figure (2) and with a bellmouth inlet installed on the model (not shown). Only data acquired at the approach condition are used in the analysis and the comparison is shown in this paper.

A one-component LDV system was used during separate wind tunnel runs to measure the axial and tangential components of velocity downstream of the fan. The rotor tangential position corresponding to each velocity measurement was determined using a once-per-rev signal fed into a shaft angle encoder. The encoder divided each rotor revolution into 900 angular bins. For the 18 bladed fan this corresponds to 50 bins per blade passage. Each time a velocity measurement was made the rotor position was determined by sampling the output of the angle encoder. Typically some 42,000 velocity measurements would be obtained at each radial-axial location from which passage averaged (periodic) velocity profiles could be constructed. The reduction process from raw data to average profiles is illustrated in figure (3).

Consider the raw data for axial component of the velocity at station 1 and at 35% span(radial) location shown in figure (3a). Note that, the abscissa in this figure, labeled the rotor position, can be equivalently treated as time or tangential location. The first step in the reduction process is to compute the once-per-rev average of the velocities occurring within each of the 900 bins. Figure (3b) shows the resulting once-per-rev average velocity distribution. The next step is to average the once-per-rev average velocity distributions that include all of the 18 blade passages into one representative passage. This process smooths out blade-to-blade variations in the flowfield that might have occured due to manufacturing differences in the blade. The result, which may be called a passage-averaged representation, is shown in figure (3c). Note that, at this point both the incoherent part of the velocity field (i.e., turbulence) and any coherent part that is locked to one rotor revolution have been taken out of the velocity data.

Contour plots of the passage-averaged axial and tangential velocities are shown in figure (4). The view is from downstream looking upstream with the fan rotating clockwise. The passage contours have been repeated to illustrate the periodic transition from one passage to another. Low velocity areas appear as dark regions while high velocity areas appear as bright regions. These contours provide an overall view of the variations of the rotor flowfield in axial, radial and tangential directions. In particular, at a given axial station and a fixed radial position, the tangential variations clearly show wakes of the fan blades. In order to use the theory developed in the previous section, the passage-averaged flowfield needs to be further separated into a mean component and a perturbation component. The mean part at each axial-radial position is obtained by a circumferential average of velocity components. The perturbation part is then simply what remains once the mean is subtracted out. Finally, in accordance with the normal mode representation discussed in the previous section, the perturbation part is Fourier-decomposed into its constituent harmonics.

Data-Theory Comparisons

Before proceeding with the comparisons, it is worth analyzing the nature of the measured mean flow variations. The mean axial and swirl components are shown in figure (5a). As noted earlier, only results for the approach condition (i.e. 5,200 RPM) will be presented in this paper. Both the

axial and swirl components show marked variations with the radius as well as the axial locations downstream of the fan. This clearly demonstrates the inadequecies of the uniform mean flow assumption often used in modeling the wake evolution behind a fan. The observed variations are mainly due to flowpath contraction (see figure (2)). The viscous effects also contribute to the variations, but are likely to have only a small influence for the axial distances considered here. The distribution of λ is shown in figure (5b), which indicates that the wake is a stable bounded perturbation. Equation (11) shows that the wake defect magnitude is modulated with an envelope of wavelength $\frac{\lambda}{U_x}$.

The first Fourier harmonic (i.e., $m = 18$) of the measured axial and tangential perturbations are shown in figure (6). For these components, there is a significant drop in the amplitude of the harmonic between locations 1 and 2 everywhere along the radius. The corresponding change between locations 2 and 3 is much smaller except near the tip. Viscous decay notwithstanding, the disproportionate changes between locations 1 and 2 as compared with the changes between locations 2 and 3, is likely caused by the proximity of location 1 to the rotor trailing edge which is only 30% of the chord upstream. The change in the structure of the harmonic between locations 1 and 2 indicates that there are significant flow variations in the tangential as well as the axial directions. A similar effect has been predicted in the theoretical analysis of reference [10] and the numerical predictions of reference [11]. It is important to note the radial redistribution of the tangential component as it evolves downstream (the harmonic appears to decay for $r > r_m$ and amplify for $r < r_m$ where $r_m = (r_{hub} + r_{tip})/2$). This effect will be shown to be caused by the mean swirl.

Using the mean and perturbation quantities obtained from the measurements as initial data, the theory described in this paper is used to predict the evolution of individual harmonic components of the perturbations as a function of the downstream distance. The results for the evolution of the first harmonic ($m = 18$) are summarized in figure (7). Slices of these 3D plots for the axial, tangential and radial components are shown in figure (8). The first three downstream locations shown correspond to the measurement locations 1, 2 and 3, while the 4th location is further downstream at 7.4 inches downstream of the fan trailing edge. A comparison between the theoretical evolution and the measured evolution for the first harmonic axial and tangential perturbation components is shown in figure (9). To obtain the complete flow field, the individual harmonics are reassembled as shown in figure (10). The complete flowfield may be used to compute the acoustics [5].The descrepencies between the measured and predicted evolutions for the $m = 18$ harmonic component (see figure (9) may be explained as follows.

First, since only axial and tangential velcoity components were measured, the initial distributions of the radial velocity and pressure perturbations must be artificially imposed on the govening equations. Therefore, any errors in this specification are likely to persists (or even grow) as the perturbations evolve dowsntream of the location 1. To ensure a proper and consistent specification of initial data, therefore, it is important to have knowledge of all three velocity component perturbations as well as the pressure perturbation. More will be said about this later.

Second, as was mentioned before, the influence of the unsteady potential field of the rotor on the locations near the fan trailing edge is not included in the theory. Hence, any such influence is missing from the evolution equations. There are experimental evidence (see reference [9]) that a significant decay can occur in the amplitude of the wake for $x/c < 0.6$ due to the fan potential flow interference effects.

Returning to the data-theory comparisons shown in figure (9), note that swirl mainly affects the disturbances near the tip section where the mean flow has large gradients. This can also be seen by observing the variation of λ shown in figure (5b). The predicted tangential perturbations are seen to have the same characteritics as those that were experimentally measured with a redistribution occuring around $r \sim r_m$, as seen in the inset of figure (8b).

The predicted radial component of perturbation is seen to amplify essentially monotonically as a function of downstream distance near the tip. Since, no measurements were taken for the radial component of the velocity, it is not possible to as-

sess this effect by comparison with data. There is, however, some evidence that the radial perturbation component is at least as large as those of the other two perturbation components lending some support to the predicted results [13, 14].

To demonstrate the importance of having a consistent set of initial data, calculations were carried out using an assumed initial profile of the radial perturbation at $x = 0$ (i.e., locatin 1). The profile used in this calculation corresponds to the one obtained at location 4 in the previous calculation. The resulting evolutions show significant difference compared with those for the zero initial radial perturbation case as shown in figure (11), although the effect of the swirl at the tip section is similar between the two cases. It is remarkable that the radial perturbations do not amplify anymore in contrast to the results shown in figure (8c).

We now examine the effect of modifying both the homogeneous pressure and radial velocity conditions at the inlet. The results show significant differences with the data and the other two cases. This only serves to emphasize the importance of a consistent and compatible set of initial data containing all three velocity components and pressure distributions at $x = 0$.

The specification of pressure perturbations at the inlet raises an important question regarding the boundary conditions imposed on ϕ for the numerical solution. One might specify the pressure perturbations (as was done above), or one might choose to specify a derivative conditions such as $\frac{\partial p}{\partial x} = 0$. The effect of the latter condition, which may be more realistic from a physical point of view, however, is rather small. This is expected because the vortical modes have a very small pressure content in them as pointed out in [4, 8] since these perturbations are nearly convected.

At the exit of the computational domain, different numerical conditions were tested.

1. $\frac{\partial p}{\partial x} = -\rho_o U_x \left(\frac{\partial^2 \psi}{\partial x^2} + i\alpha \frac{\partial \psi}{\partial x} \right) e^{i\sigma} = 0,$
2. $\frac{\partial^2 \psi}{\partial x^2} = 0,$
3. $\frac{\partial^2 \psi}{\partial x^2} + \frac{\lambda^2}{U_x^2} \psi = 0.$

The first condition is a common condition used in typical CFD calculations. The second condition is a weaker form of the first condition and is tested to check the importance of the term $\frac{\lambda^2}{U_x^2}\psi$ in the third condition. The third condition is based on the physical argument that the pressure perturbation is modulated by a wavelike structure with $\frac{\lambda}{U_x}$ representing the associated wavenumber. The results of the analysis indicate that:

1. The decay of the modes at the tip section was less for the first condition than the third.
2. The choice of the second condition showed nearly the same results as those in the first with very little noticeable differences.
3. The third condition yielded a smooth pressure profile at the exit.
4. For all cases, the solutions showed similar basic trends with only small difference in details. This lends support to the argument that the flow is a nearly convected flow as shown in [4, 8].
5. It may be concluded that the choice of the most physical condition is best for this type of evolution problem as was also suggested in [4].

Conclusions

The theory developed by Golubev and Atassi [4] was generalized to account for arbitrary radial distributions of mean swirl in modeling the evolution of rotor wakes. Using experimentally meassured flow data as mean flow and initial condition inputs, the theory was used to predict the evolution of the wake perturbations as a function of distance downstream of the fan. Comparisons with measured wake evolutions on a harmonic basis indicate that swirl has a significant effect where large radial mean flow gradients occur. It appears that, for the most part, the radial and tangential perturbations exchange momentum as the perturbation field evolves downstream.

The theory was unable to model the significant change between locations 1 and 2 as seen in the data. This may be attributed to the proximity of the measurement location 1 to the fan trailing edge where unsteady potential effects of the fan may be significant.

The effects of different inlet and outlet conditions on the evolution were also analyzed. It appears that the results are sensitive to the inlet conditions, but that outlet conditions play only a small role. This supports the normal mode analysis which indicate that the vortical perturbations have inly a small pressure content associated with them.

References

[1] Atassi, H.M., *Unsteady aerodynamics of vortical flows; early and recent developments*, Symposium on Aerodynamics, World Scientific, 1993.

[2] Meyer, H.D. and Envia, E., *Aeroacoustic Analysis of Turbofan Noise Generation*, NASA CR-4715, 1996.

[3] Kerrebrock, J.,L., *Small disturbances in turbomachine annuli with swirl*, AIAA Journal, Vol. 15, p. 794-803, 1977.

[4] Golubev, V. and Atassi, H.M., *Interaction of unsteady swirling flows with annular cascades. Part I. Evolution of incident disturbances*, to appear in AIAA Journal, 2000.

[5] Golubev, V. and Atassi, H.M., *Interaction of unsteady swirling flows with annular cascades. Part II. Aerodynamic blade response*, To appear in AIAA Journal, 2000.

[6] Golubev, V. and Atassi, H.M., *Sound propagation in an annular duct with meanpotential swirling flow*, Journal of Sound and Vibration, Vol. 198, p. 601-616, 1996.

[7] Golubev, V. and Atassi, H.M., *Acoustic-vorticity waves in swirling flows*, Journal of Sound and Vibration, Vol. 209, p. 203-222, 1998.

[8] Ali, A., Atassi, H.M., Atassi, O., *Acoustic Eigenmodes in a Coannular Duct with a General Swirling Flow*, 6th AIAA/CEAS Aeroacoustics Conference and Exhibit, AIAA 2000-1954.

[9] Lakshminarayana, B. and Davino, R., *Mean velocity and decay characteristics of the guidevane and stator blade wake of an axial flow compressor*, Transactions of ASME, Vol. 102, p. 50-60, 1980.

[10] Scherock, J.,J., *Modeling of unsteady potential flows in coupled cascades*, MSc. Thesis, University of Notre Dame, 1996.

[11] Sekularac, A., Falk, E.A., Jumper, E. and Haven B., *A conformal mapping analysis of cascade trailing-edge flows*, AIAA 2000-0229.

[12] Ravindranath, B. and Lakshminarayana, B., *Three dimensional and turbulence characteristics of the near wake of a compressor rotor blade*, NASA Contractor Report 159518, June 1980.

[13] Ulrich Ganz, *Experimental investigation of the unsteady flow characteristics in the Boeing 18 inch fan rig*, AIAA99-1886, p.598-612.

[14] Hsu, S.T. and Wo, A.M., *Near-wake measurements in a rotor/stator axial compressor using slanted hot-wire technique*, Experiments in Fluids, Vol. 23, p. 441-444, 1997

[15] Woodward, R.P., Elliott, D.L., Hughes, C.H., and Berton, J.J., *Benefits of Swept and Leaned Stators for Fan Noise Reduction*, AIAA-99-0479, NASATM-208661, November 1998.

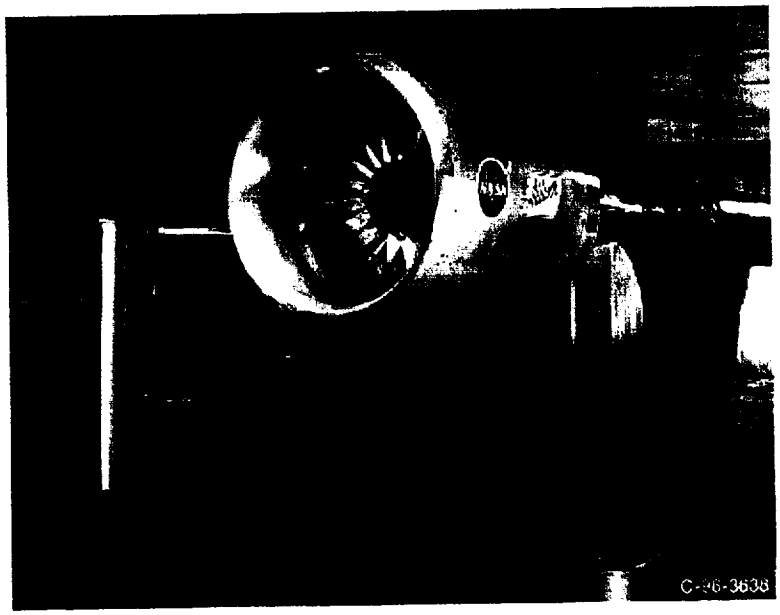

Figure 1: Allison Low Noise fan model in 9-foot x 15-foot NASA Glenn Low Speed Wind Tunnel

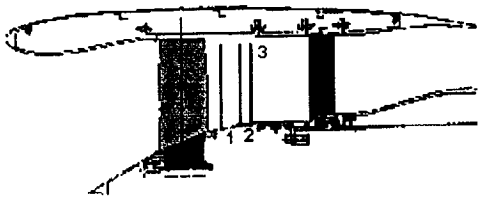

Figure 2: Schematic of flow path and axial locations of LDV measurements

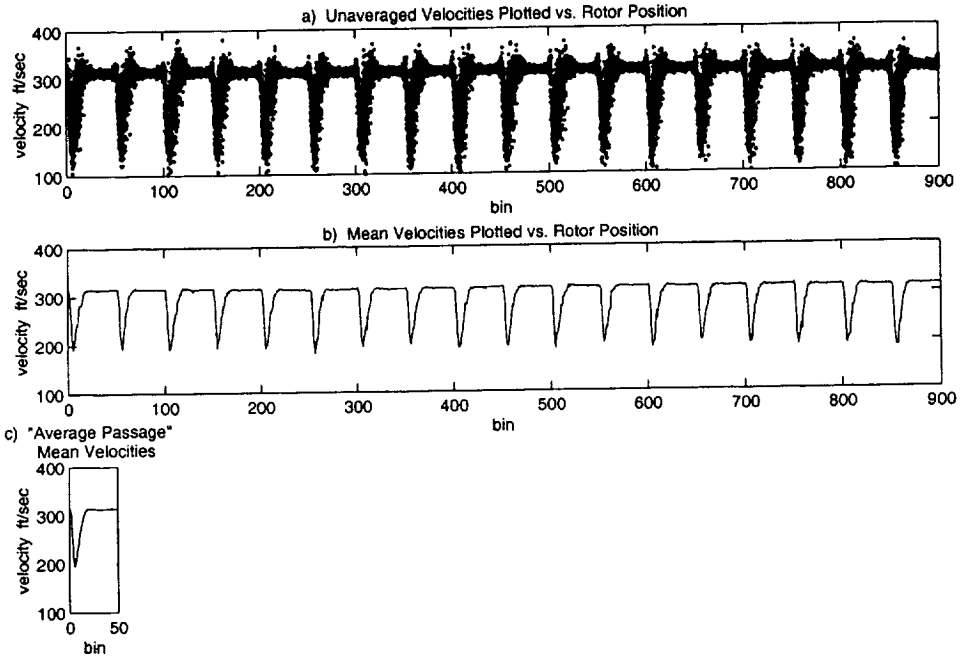

Figure 3: Illustration of LDV data reduction process

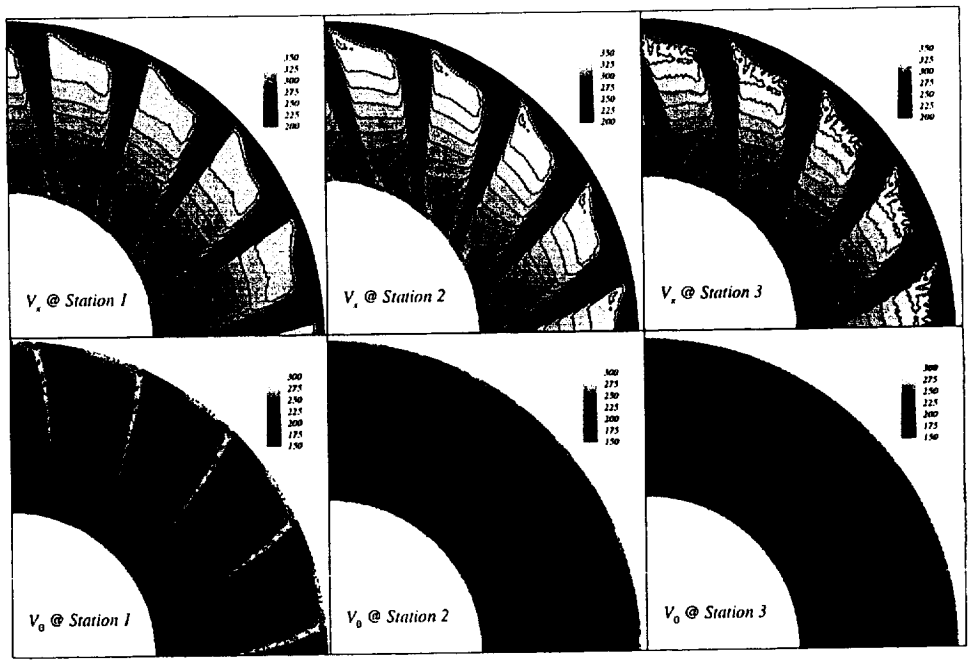

Figure 4: Contours of passage-averaged flowfields at axial stations 1, 2 and 3

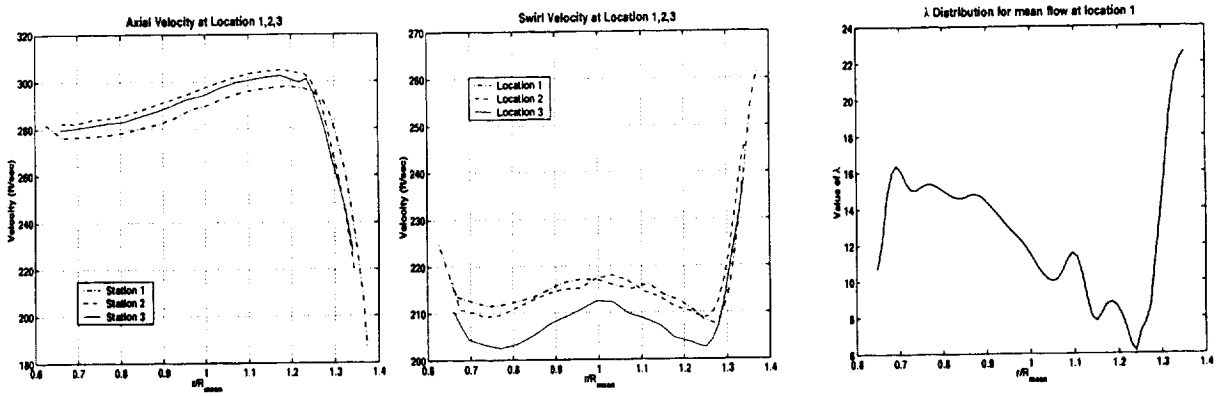

(a) Axial and Swirl Velocity

(b) λ computed at location 1

Figure 5: Mean Flow Characterisitics

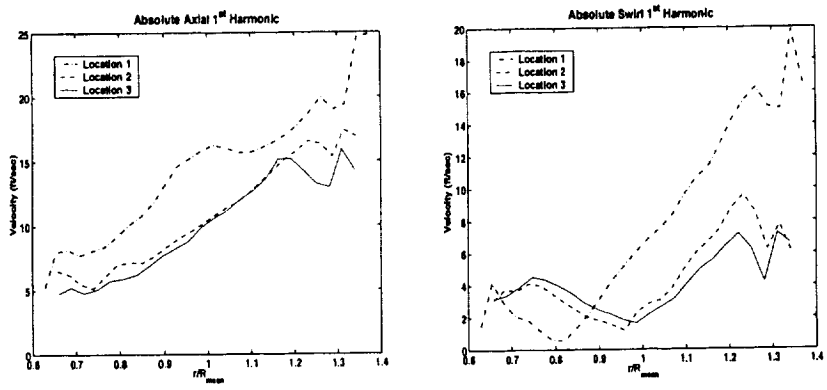

(a)

(b)

Figure 6: 1^{st} Fourier mode ($m = 18$) for axial and swirl velocity components

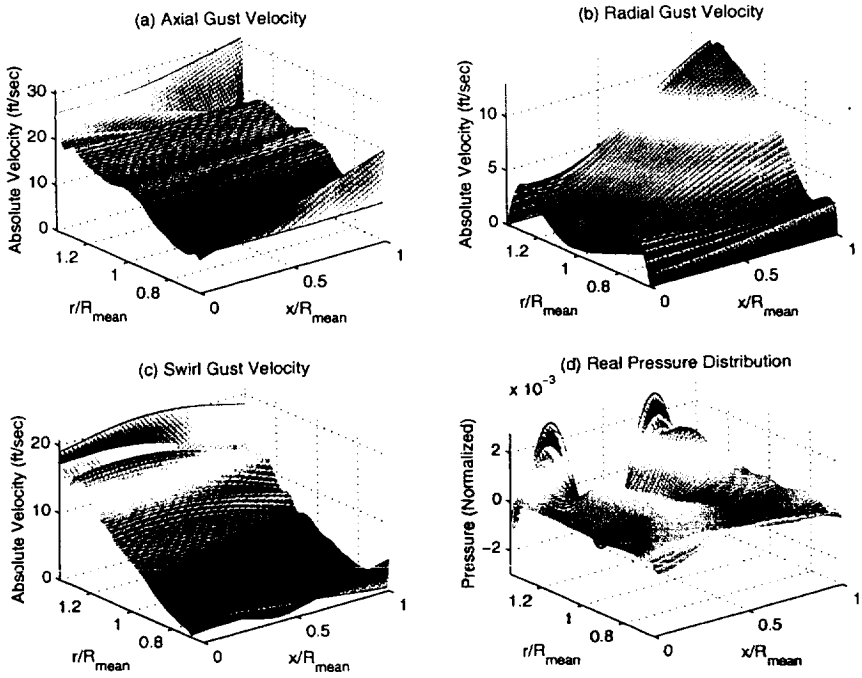

Figure 7: Numerical Simulation

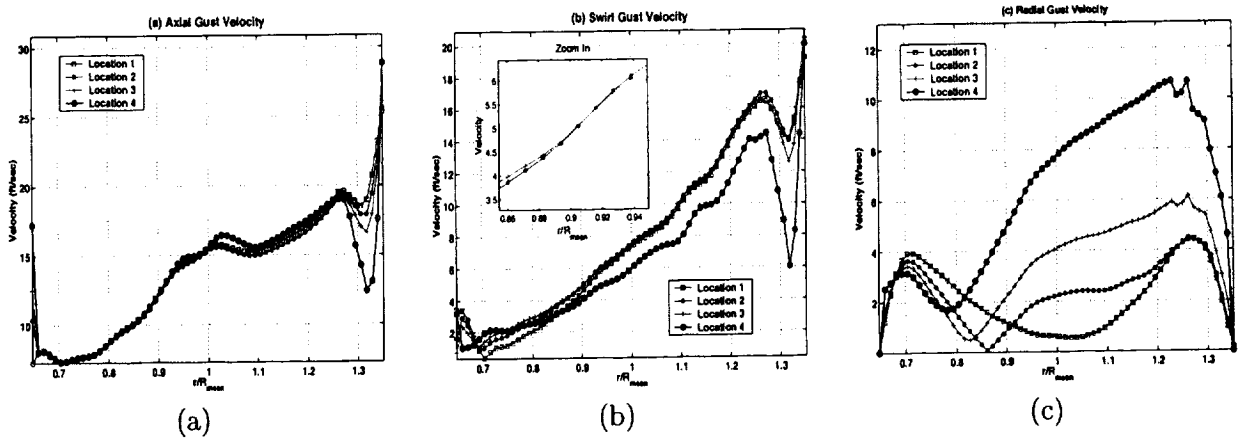

(a) (b) (c)

Figure 8: 1^{st} Fourier mode evolution for the axial, swirl and radial velocities.

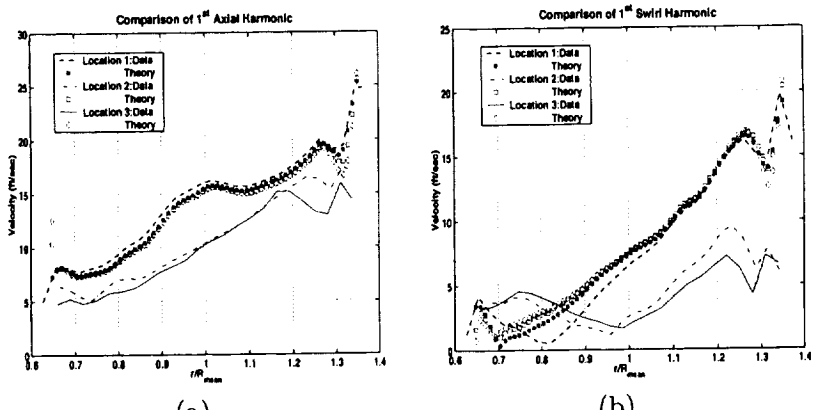

(a) (b)

Figure 9: Comparison between the present theory and measured data

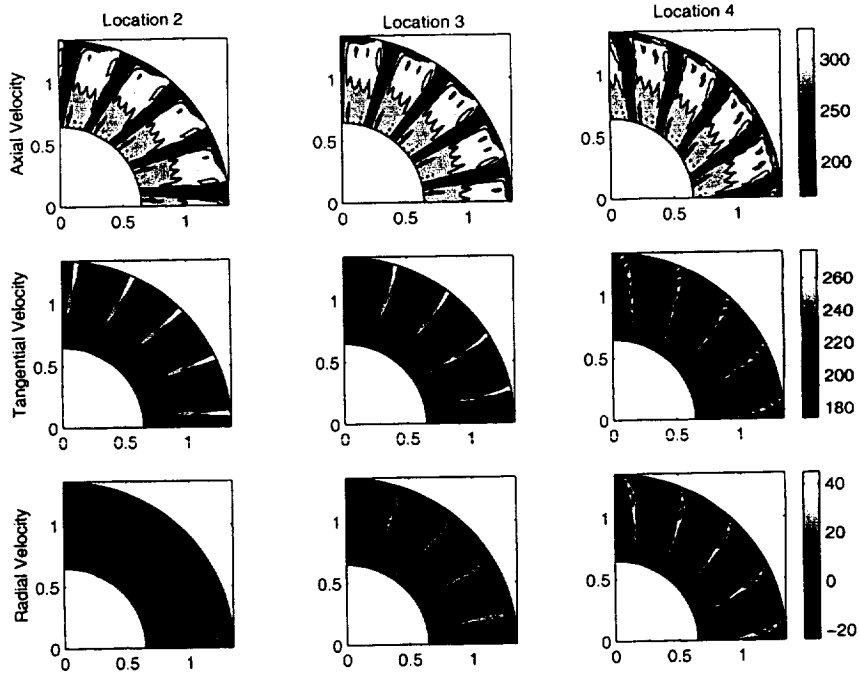

Figure 10: Wake reconstruction downstream

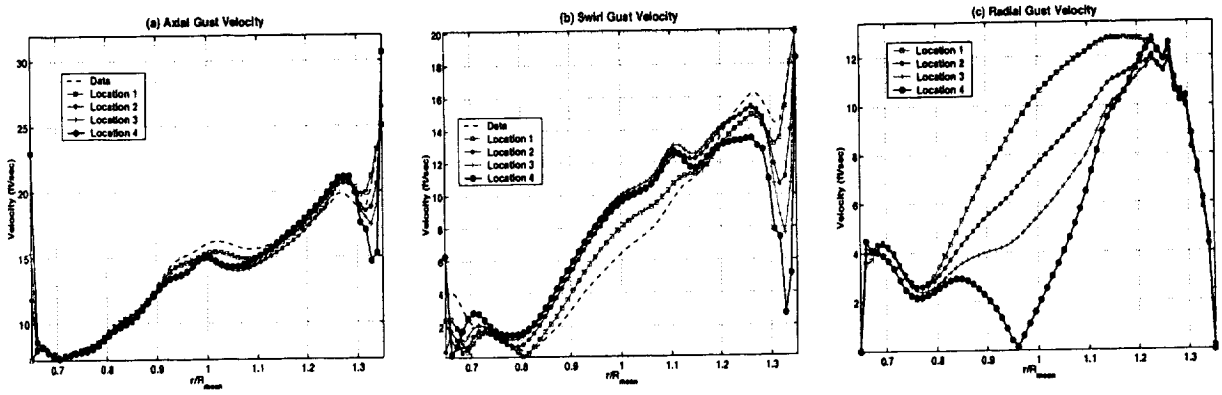

(a) (b) (c)

Figure 11: 1^{st} Fourier mode evolution for axial, swirl and radial perturbations